

# Substitutional or Interstitial Site-Selective Nitrogen Doping in TiO<sub>2</sub> Nanostructures

Jared Lynch,<sup>†,‡</sup> Cinzia Giannini,<sup>§</sup> Jason K. Cooper,<sup>†,‡</sup> Anna Loiudice,<sup>†,‡</sup> Ian D. Sharp,<sup>†,||</sup> and Raffaella Buonsanti<sup>\*,†,‡</sup>

<sup>†</sup>Joint Center for Artificial Photosynthesis, Lawrence Berkeley National Laboratory, Berkeley, California 94720, United States

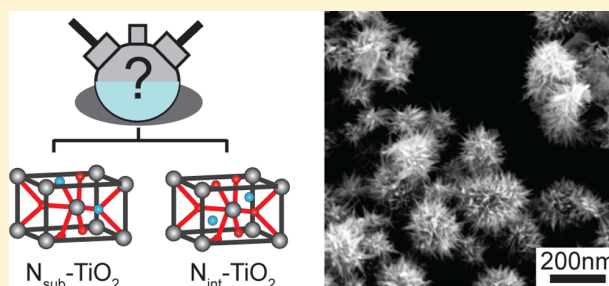
<sup>‡</sup>Lawrence Berkeley National Laboratory, Materials Science Division, One Cyclotron Road, Berkeley, California 94720, United States

<sup>§</sup>Istituto di Cristallografia, National Research Council of Italy, via Amendola 122/O, Bari, 70126, Italy

<sup>||</sup>Lawrence Berkeley National Laboratory, Physical Biosciences Division, One Cyclotron Road, Berkeley, California 94720, United States

## Supporting Information

**ABSTRACT:** Herein, we report a colloidal wet-chemical approach enabling control on dopant concentration and location in a nanocrystal host lattice. Growth-doping and nucleation-doping, driven by primary and tertiary amines, respectively, were identified as predominant doping mechanisms responsible for the introduction of nitrogen impurities in interstitial and substitutional sites in highly branched rutile TiO<sub>2</sub> nanostructures. High-resolution X-ray photoelectron spectroscopy was used to distinguish the two nitrogen occupational lattice sites and, in combination with UV–vis absorption spectroscopy, to investigate the impact of the nitrogen impurities on the optoelectronic properties. The implementation of the nitrogen-doped titania nanostructures in photoelectrodes for water oxidation suggests that these atomically defined building blocks can function as a platform to investigate the impact of the nitrogen occupational sites on the photocatalytic properties. By deliberately choosing precursors and reaction conditions, instead of relying on the most common high temperature annealing of preformed metal oxide in ammonia, we emphasize the importance of understanding the chemistry behind doping to achieve an unprecedented level of control on effective dopant introduction and, therefore, property tunability.



## INTRODUCTION

New and distinctive optoelectronic properties emerge when dopants are introduced in inorganic nanocrystals instead of their bulk counterparts.<sup>1–12</sup> Not only dopant concentration but also their location in the host lattice (i.e., substitutional vs interstitial, surface vs bulk) has been shown to impact significantly the deriving properties; yet positioning dopants in specific lattice sites still remains a synthetic challenge.<sup>1–12</sup> For example, localized surface plasmon resonances in metal oxides arise from n-type doping, which requires actual substitution of the host cation with the dopant cation in a higher valence state (i.e., In<sup>3+</sup> with Sn<sup>4+</sup> in tin-doped indium oxide, Zn<sup>2+</sup> with Al<sup>3+</sup> in aluminum-doped zinc oxide).<sup>7–10</sup> In these systems, doping concentration modulates the plasmon resonance frequency, while the spatial distribution in the nanocrystal volume (surface segregated vs homogeneously distributed) influences the quality factor of their plasmon resonance.<sup>8</sup> In a second example, concentration-dependent positioning of silver impurities in interstitial or substitutional lattice sites has been shown to infer n-type or p-type character to cadmium selenide nanocrystals, respectively.<sup>3</sup> As a last example, in upconverting nanocrystals, the spatial distribution

and local relative concentration of dopants is essential to engineer their optical properties and enhance their upconverting efficiency.<sup>11,12</sup>

Among different heteroatoms, nitrogen dopants have been widely used to modify the electronic structure and to extend the absorption of metal oxide photocatalysts to the visible range.<sup>13–18</sup> Narrowing the band gap of earth-abundant wide-band gap metal oxide photocatalysts to increase their visible light absorption is critical to advancing their applications in solar-to-fuel energy conversion. In the case of nitrogen-doped metal oxides, and oxynitrides more generally, only the actual substitution of O<sup>2-</sup> by N<sup>3-</sup> with high N concentrations results in the desired band gap narrowing by elevating the valence band edge.<sup>16,18</sup> Furthermore, the position of nitrogen dopants with respect to the surface has been shown to impact the photoconversion efficiency as well as the water oxidation reaction decomposition pathway.<sup>19,20</sup> Recently, first-principles calculations have identified a series of ternary and quaternary

**Received:** December 22, 2014

**Revised:** March 4, 2015

**Published:** March 4, 2015

oxynitrides (e.g.,  $\text{Ti}_3\text{O}_3\text{N}_2$ ,  $\text{La}_2\text{TiO}_2\text{N}_2$ , and  $\text{Li}_3\text{MoO}_4\text{N}$ ) that are particularly promising as visible-light-driven photocatalysts because of their predicted band gap (around 2 eV) and band edge positions which are suitable for water splitting.<sup>16</sup> To move toward these complex multielement materials, it is important to establish meaningful insights into the chemistry governing their composition and atomic spatial distribution.

In the present work, we focus on site-selective nitrogen incorporation into titania nanostructures. The vast amount of literature on nitrogen-doped titanium dioxide (N-TiO<sub>2</sub>) provided us a knowledge base for unambiguous verification of our synthetic approach through established spectroscopic methods.<sup>21–31</sup> By starting from this relatively simple and well-studied system, we were able to get insights into the mechanism of substitutional versus interstitial nitrogen incorporation. This gained knowledge is expected to inform the development of next generation, likely ternary and quaternary, oxides and oxynitrides. Furthermore, we note that this material system, and engineering of its defects, remains of considerable interest to the scientific community.<sup>17,32–35</sup> Surprisingly, to date, the most common approach to synthesize N-TiO<sub>2</sub> thin films and powders still consists of high-temperature ( $\geq 600$  °C) annealing of preformed TiO<sub>2</sub> in ammonia atmosphere.<sup>13,22,26,31</sup> Using this doping approach, low nitrogen content is usually achieved (<2%) and poor control on the nitrogen atom location in the lattice can be exerted. Moreover, particularly in the case of nanocrystalline TiO<sub>2</sub>, sintering and grain growth can result from performing high temperature annealing for several hours. A few attempts of postsynthetic room temperature amination reactions using short chain amines have been pursued; however, mainly interstitial nitrogen has been introduced and no conclusive proof of the presence of nitrogen across the crystal volume has been provided.<sup>36–39</sup>

Herein, we demonstrate a solution-based approach to the synthesis of N-TiO<sub>2</sub> nanostructures based on colloidal chemistry where the nitrogen concentration and the dopant host lattice environment are controlled. By revealing the different role played by primary versus tertiary amines in the nitrogen doping mechanism, we developed a means to manipulate the dopant environment between interstitial ( $N_{\text{int}}$ ) and substitutional ( $N_{\text{sub}}$ ) while accessing nitrogen concentrations ranging from 2 to 17 at. %. High resolution X-ray photoelectron spectroscopy (XPS), scanning and transmission electron microscopy (SEM, TEM), nuclear magnetic resonance spectroscopy (NMR), wide-angle X-ray diffraction (XRD), and UV–visible absorption spectroscopy (UV–vis) confirmed the effective and controlled incorporation of  $N_{\text{int}}$  or  $N_{\text{sub}}$  in our TiO<sub>2</sub> nanostructures. By establishing how to intentionally tune the position of N dopants in the TiO<sub>2</sub> nanocrystal host lattice, we create a platform that provides opportunities for understanding and tuning the optoelectronic and photocatalytic properties of this material, thus highlighting the importance of atomic-level chemical manipulation of doping and alloying to build meaningful structure/property relationships.

## EXPERIMENTAL SECTION

**Materials.**  $\text{TiCl}_4$  (99.9%), sodium amide ( $\text{NaNH}_2$ , >90%), oleylamine (OAm, technical grade, 70%), trioctylamine (TOA, 98%), oleic acid (OLA, technical grade, 90%), 1-octadecene (ODE, tech. grade, 90%), squalene (SQA, >98%), trihexylamine (THA, 96%), hexane, toluene, chloroform, methanol, acetonitrile (ACN, >99.9%), trimethyloxonium tetrafluorobo-

rate ( $\text{Me}_3\text{OBF}_4$ , 95%), potassium hydroxide (KOH, >85%), deuterium chloride solution (35% wt. DCl in D<sub>2</sub>O, 99% D), and deuterium oxide (D<sub>2</sub>O, 99.9% D) were all purchased from Sigma-Aldrich and used as received. Dodecylamine (DDA, 98%) was purchased from Fluka. Standard rutile titanium dioxide (TiO<sub>2</sub>, 99.9%) was purchased from Alfa Aesar and used after grinding with a mortar and pestle and dispersing in reagent alcohol.  $\text{TiCl}_4$  and  $\text{NaNH}_2$  were stored in a nitrogen filled glovebox.

**Synthesis of N-TiO<sub>2</sub> Nanostructures.** All syntheses were carried out under air-free conditions using a standard Schlenk line setup. Two stock reactant solutions of  $\text{TiCl}_4$  (220  $\mu\text{L}$ ,  $\sim 2$  mmol in 1 mL of ODE) and  $\text{NaNH}_2$  (80 mg,  $\sim 2$ –6 mmol in 1 mL of ODE) were prepared in a nitrogen glovebox using previously degassed ODE. As a general synthetic procedure, 16 mL of a squalene/amine mixture (where the amine concentration was varied from 0.2 M to 0.6 M to pure amine) and 30  $\mu\text{L}$  of OLA ( $\sim 0.1$  mmol) were loaded into a 50 mL three-necked flask and degassed first at room temperature for 15 min and then 120 °C for 1 h. At this point, the  $\text{TiCl}_4$  solution followed immediately by the  $\text{NaNH}_2$  solution were injected and the temperature was raised to reflux near 300 °C at a ramp rate of 10 °C/min. After 5 h at reflux, the reaction was halted by removing the heating mantle. The N-TiO<sub>2</sub> samples were washed three times using chloroform and excess methanol. Finally, they were rinsed additional times using a 1:1 v:v ratio of hexanes and toluene to remove any residual organometallic complexes. The N-TiO<sub>2</sub> nanocrystals were stored as suspensions in hexane prior to characterization. To study the effect of the amine type on the nanostructure growth and doping mechanism, oleylamine and dodecylamine were chosen as primary amines while trioctylamine and trihexylamine as tertiary amines.

**Characterization.** Transmission electron microscopy images were recorded on an Analytical JEOL-2100F FETEM using a beam energy of 200 kV, equipped with a Gatan camera. Samples were drop casted on a lacey holed carbon TEM grid (Ted Pella, Inc.) prior to imaging.

Scanning electron microscopy images were acquired on a Zeiss Gemini Ultra-55 Analytical Scanning Electron Microscope using a beam energy of 5 kV and an in-lens detector. Samples were drop casted on a silicon substrate prior to imaging.

Wide-angle X-ray diffraction was performed on a Bruker Gadds-8 diffractometer with a Cu  $K\alpha$  source operating at 40 kV and 40 mA. Samples were drop-casted on glass microscope slides prior to measurement. Rietveld analysis was performed by using a whole-profile Rietveld-based fitting program.<sup>45</sup> The XRD patterns were modeled by a mixture of anatase (space group  $I41/amd$ ; cell parameters:  $a = b = 3.7835430$  Å and  $c = 9.614647$  Å;  $\alpha = \beta = \gamma = 90^\circ$ ), brookite (space group  $Pbca$ ; cell parameters:  $a = 9.166$  Å,  $b = 5.411$  Å, and  $c = 5.149$  Å;  $\alpha = \beta = \gamma = 90^\circ$ ), and rutile (space group  $P42/mnm$ ; cell parameters:  $a = b = 4.59365$  Å and  $c = 2.95874$  Å;  $\alpha = \beta = \gamma = 90^\circ$ ) crystalline structures. The analysis allowed determination of the weight fraction of each crystalline phase in the mixture along with the cell parameters.

X-ray photoelectron spectroscopy was performed using a monochromatized Al  $K\alpha$  source ( $h\nu = 1486.6$  eV), operated at 225 W, on a Kratos Axis Ultra DLD with a pass energy for narrow scan spectra of 20 eV, corresponding to an instrument resolution of approximately 600 meV. Survey spectra were collected with a pass energy of 80 eV. Unless otherwise noted,

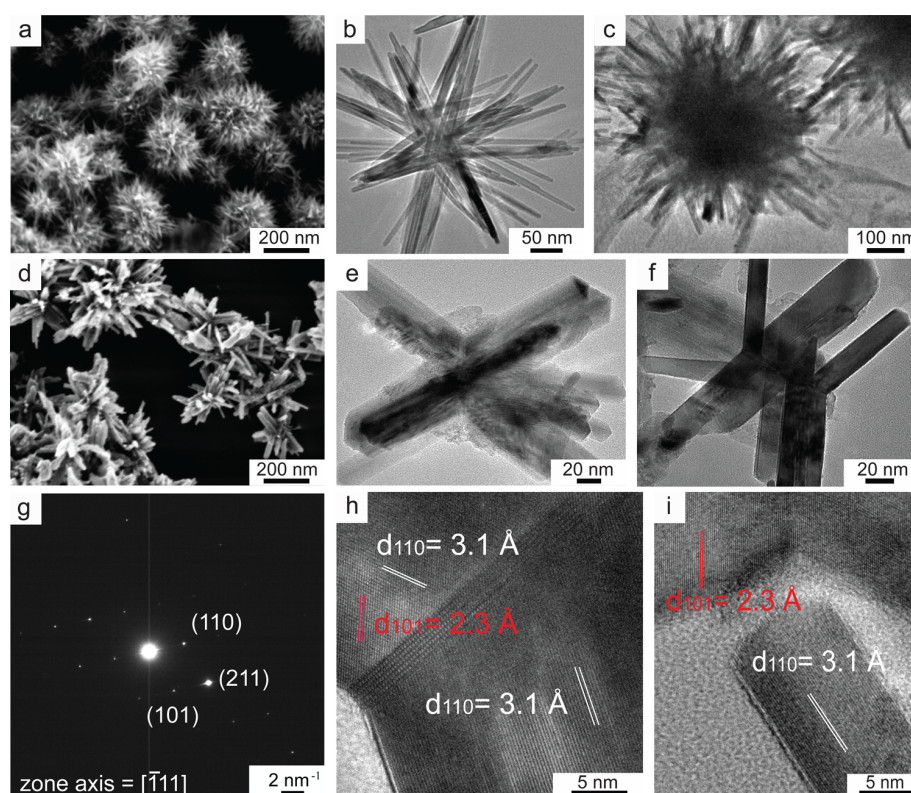


**Figure 1.** (a, d) Top-view SEM and (b, c, e, f) low magnification TEM images of N-TiO<sub>2</sub> NU samples synthesized in OAm (a–c) and in TOA (d–f). (g) SAED pattern of a single N-TiO<sub>2</sub> NU branch. (h, i) HRTEM images of N-TiO<sub>2</sub> NUs grown in pure TOA (h) and OAm (i).

measurements were performed at a takeoff angle of 0° relative to the surface normal. Spectral fitting was performed using Casa XPS analysis software. Spectral positions were corrected by shifting the primary C 1s core level position to 284.8 eV, and curves were fit with quasi-Voigt lines following Shirley background subtraction. Samples were deposited on conductive Si substrates. To minimize the possibility of the amine ligands contributing to the nitrogen signal, all XPS samples were chemically stripped of their surface ligands using the well-established Meerwein salt procedure followed by thermal annealing at 500 °C for 1 h under an inert atmosphere.<sup>40</sup> As shown in Figures S6–S8 (Supporting Information), no morphological and compositional changes were observed after treatment. We define  $N_{\text{tot}} = [N/(N + O)] \times 100$  and  $N_{\text{sub}}/N_{\text{tot}} = [N_{\text{sub}}/(N_{\text{sub}} + N_{\text{int}})] \times 100$ . We set  $(N + O) = 2\text{Ti}$  based on stoichiometric consideration. A rigorous quantification of oxygen by XPS is hindered by the adsorbed water and oxygen-bearing groups in carbon contaminants contributing to the signal. The analysis of Ti is accurate instead, thus justifying the choice of calculating  $N_{\text{tot}}$  based on the Ti content in the samples.

Samples for combustion analysis were prepared with purified N-TiO<sub>2</sub> nanostructures, as described above, that had been dried overnight to remove all solvent. Samples were measured on a PerkinElmer 2400 Series II combustion analyzer equipped for determination of % C, % H, and % N.

<sup>1</sup>H spectra NMR spectra were obtained using a Bruker AVANCEIII 500 instrument, and peaks were referenced to the residual H<sub>2</sub>O peak. To capture the evolving gas from the reaction mixture, the nitrogen carrier gas was collected downstream through a fritted glass bubbler containing 5 mL

of deuterium chloride solution 35% in D<sub>2</sub>O (Aldrich). NH<sub>3</sub> was captured as soluble NH<sub>4-x</sub>D<sub>x</sub>Cl and detected by NMR spectroscopy.

Attenuated total reflectance Fourier transform infrared spectroscopy (ATR-FTIR) was performed using a Bruker Platinum ATR accessory with a diamond ATR crystal installed in a Bruker Vertex 70. Samples were dropcast on the diamond crystal to ensure effective optical coupling. Spectra were collected from reaction aliquots and measured directly after in air with a 4 cm<sup>-1</sup> resolution, GloBar MIR source, a broadband KBr beamsplitter, and a liquid nitrogen cooled MCT detector. Background measurements were obtained from the bare diamond plate.

Ultraviolet–visible absorption spectroscopy diffuse reflectance spectra were recorded on a Shimadzu SolidSpec-3700 spectrometer with a D<sub>2</sub> (deuterium) lamp for the ultraviolet range and a WI (halogen) lamp for the visible and near-infrared. Measurements were performed with an integrating sphere. Samples were deposited on glass microscope slides. Kubelka–Munk transformations were made on diffuse reflectance spectra using the UVProbe software.

For the photoelectrochemical measurements, electrodes were prepared by drop casting N-TiO<sub>2</sub> nanostructures dispersed in solution on FTO-coated glass substrates (~1 × 1 cm<sup>2</sup>). Next, the films were stripped of their ligands by gently soaking in a Me<sub>3</sub>OBF<sub>4</sub> solution (40 mM in acetonitrile) for 10 min followed by rinsing in a 1:1 chloroform to acetonitrile solution inside a glovebox, as reported by Rosen et al.<sup>40</sup> After annealing of the film under a nitrogen atmosphere inside a tube furnace at 500 °C for 1 h, the as-prepared electrodes were connected to a copper wire using conductive silver epoxy (SPI supplies).

Afterward, the entire substrate, except for the front side with the N-TiO<sub>2</sub> nanostructures, was covered by nonconductive hysol epoxy (Loctite) to electrically isolate the leads from electrolyte and prevent dissolution of the silver paste in solution. Photoelectrochemical (PEC) measurements were conducted using a CHI 604D Potentiostat/Galvanostat in a three-electrode configuration: N-TiO<sub>2</sub> nanocrystal film as the working electrode, a Pt wire as the counter electrode, and an Ag/AgCl in 3 M KCl as the reference electrode. The electrolyte was 1 M KOH solution. The current flowing into the photoanode was defined as positive. In a typical experiment, the potential was linearly swept from  $-0.7$  to  $0.7$  V vs Ag/AgCl at a scan rate of 20 mV/s. Other sweeping ranges, directions, and rates were also tested. The light source was an AM 1.5 solar simulator (Solar Light Co, Inc. model XPS 300) with the illumination intensity adjusted to 100 mW/cm<sup>2</sup>. A set of seven photoelectrodes was tested for each studied structure. The standard error on the photocurrent drop after inserting a cutoff filter blocking the UV light below 400 nm was within 20% of the reported values. Film processing optimization and catalyst deposition to increase photocurrent density were out of the scope of the present work but are currently under investigation.

## RESULTS AND DISCUSSION

In a typical synthesis, a titanium tetrachloride solution (TiCl<sub>4</sub>) was injected in a degassed mixture of primary or tertiary amine in squalene and oleic acid at 120 °C, followed by the injection of a sodium amide solution (NaNH<sub>2</sub>). The temperature of the reaction mixture was raised to reflux near 300 °C by slow ramping ( $\sim 10$  °C/min), and then, the reaction mixture was held at this temperature for 5 h. The size, shape, and crystallinity of the as-synthesized N-TiO<sub>2</sub> nanostructures were assessed by SEM and TEM (Figure 1 and Figures S1 and S2, Supporting Information). The nanostructures exhibited an urchin-like hyperbranched morphology with an overall size of 200 nm; they will be referred to as nanourchins (NUs) in the rest of the manuscript. The branching diameter and the degree of branching varied with the amine type. Specifically, an overall higher degree of branching and branches with smaller diameters ( $\sim 10$ – $20$  nm) were obtained with primary amines, namely, oleylamine (OAm) and dodecylamine (DDA) (Figure 1a–c and Figure S1e, Supporting Information). Tertiary amines, namely, trioctylamine (TOA) and trihexylamine (THA), generated NUs with a lower degree of branching and branches with bigger diameters (Figure 1d–f and Figure S1f, Supporting Information, branch diameter  $\sim 20$ – $40$  nm). High-resolution TEM (HRTEM) images of typical N-TiO<sub>2</sub> NUs, synthesized in OAm and TOA, and the selected-area-diffraction pattern (SAED) collected on a single branch (Figure 1g–i) revealed that a high degree of crystallinity is present across the entire length of each branch. The lattice fringes in Figure 1h and i yielded *d*-spacings of 3.1 and 2.3 Å which correspond closely to the TiO<sub>2</sub> rutile (110) [ $d_{110} = 3.25$  Å] and (101) [ $d_{101} = 2.49$  Å] *d*-spacing. Twin boundaries were identified at the branching points of the N-TiO<sub>2</sub> NUs, possibly indicating a crystal splitting mechanism (Figure 1h,i).<sup>41–45</sup> The formation of such hyperbranched spherulitic-type morphologies is usually attributed to fast growth kinetics driven by extremely high supersaturation conditions and to the presence of ions in the growing solution.<sup>41–45</sup> In agreement with crystal splitting, we observed a rapid growth rate of the N-TiO<sub>2</sub> NUs that indeed prevented us from capturing the system in the early evolution stages close to nucleation (Figure S2, Supporting Information). The high

reactivity of TiCl<sub>4</sub>, especially in the presence of a strong base and nucleophile such as NaNH<sub>2</sub>, most likely accounts for the fast kinetics. As for the morphological changes observed by varying the amine type, a possible explanation arises from the need to minimize surface energy during the nanocrystal growth. Each time a crystal splits, a new surface is created. Therefore, ligands that better passivate the crystal surface will energetically favor a structure with a higher degree of branching. More branches form, more monomers are consumed during the nucleation step, fewer monomers remain for their growth, and hence smaller diameters are obtained. As a result of their lower steric hindrance, primary amines pack more densely, thus stabilizing the nanocrystal surfaces more efficiently than tertiary amines. This reasoning explains the observation that thinner branches and a higher branching degree occur in the presence of OAm and DDA.

Through quantitative Rietveld analysis, XRD measurements confirmed the presence of rutile as the majority phase in the N-TiO<sub>2</sub> NUs (Figure 2 and Figure S3 and Table S1, Supporting Information), consistent with the HRTEM and electron diffraction data.

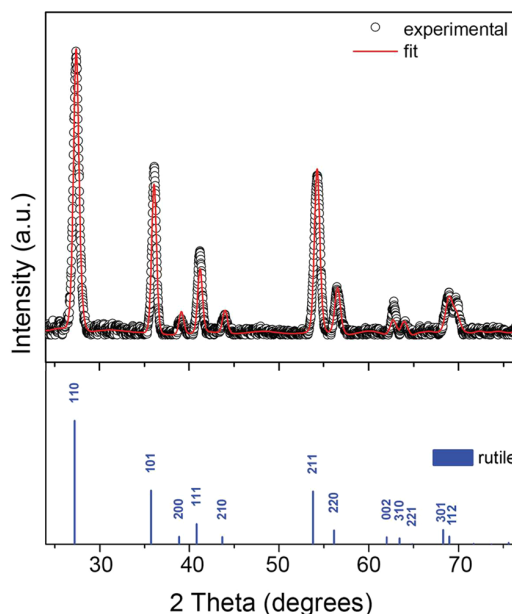


**Figure 2.** Representative XRD pattern of N-TiO<sub>2</sub> NUs synthesized in OAm along with the reference pattern of bulk rutile at the bottom (PDF 04-008-7848). The experimental curve (open circles) is compared to the corresponding Rietveld-based fit (solid red line), indicating the presence of a pure rutile phase.

The refined structural parameters pointed at a non-monotonic expansion of the rutile unit cell up to 0.6% at varied amine concentration (Table S1 and Figure S3, Supporting Information). This variation is close to what was reported in a recent comprehensive structural study on nitrogen-doped anatase TiO<sub>2</sub> nanostructures.<sup>46</sup> However, even in this case, the authors comment about the influence of the nitrogen source and other charge compensating defects (i.e., oxygen vacancies and Ti<sup>3+</sup>) on the lattice expansion.<sup>46–49</sup> Moreover, similar lattice deformations have often been assessed in nanosized metal oxide as a result of nonstoichiometry and/or strain effects.<sup>42,50</sup> Thus, at this stage, drawing any meaningful

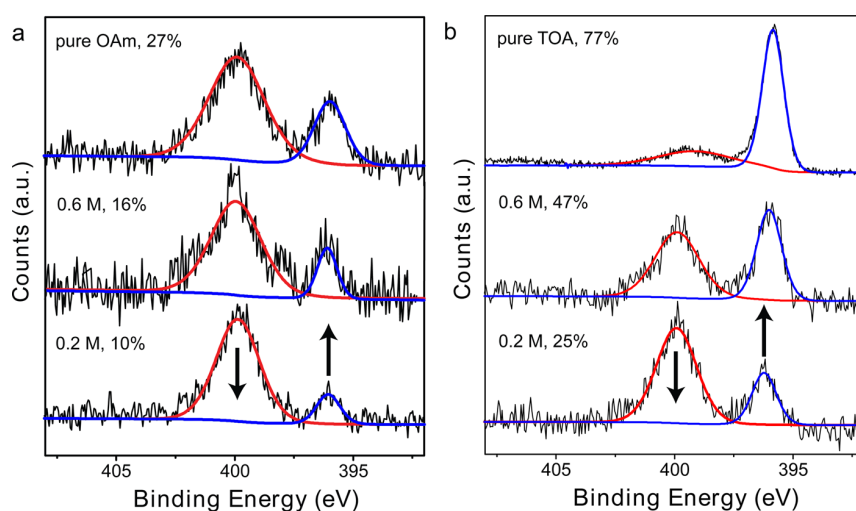


**Figure 3.** N 1s high-resolution XPS spectra of N-TiO<sub>2</sub> NUs synthesized in a reaction mixture containing (a) OAm and (b) TOA with varied concentration (from 0.2 M in squalene to amine as the solvent). The XPS spectra are fitted with two components corresponding to  $N_{\text{sub}}$  (396 eV, blue line) and  $N_{\text{int}}$  (400 eV, red line). The  $N_{\text{sub}}/N_{\text{tot}}$  percentage ratio is indicated in each panel; the arrows point at the increase of the  $N_{\text{sub}}$  component and the decrease of the  $N_{\text{int}}$  component with the increase of amine concentration.

conclusion from the observed changes in the lattice parameters at different amine content would be only speculative without additional compelling evidence indicating nitrogen presence.

XPS analysis served a critical tool to assess the nitrogen presence and to investigate its chemical state in the N-TiO<sub>2</sub> NUs (Figure 3 and Figures S1 and S4–S6 and Table S2, Supporting Information). It is noted that, although XPS is a surface sensitive technique, a significant fraction of the total volume of the N-TiO<sub>2</sub> NUs was still sampled as the branch diameters ranged between 10 and 20 nm and the particles were randomly oriented on the substrate (see the Supporting Information). In fact, combustion analysis, used as a complementary bulk technique, yielded values of  $N_{\text{tot}}$  that were in agreement with the XPS values within a few percent of error. Prior to XPS measurements, as described in more detail in the Experimental Section, ligand removal was accomplished by reactive chemical stripping and sample annealing was performed to exclude any spectral contribution of the amine ligands.<sup>40</sup> The thermal annealing conditions were chosen to ensure sample morphology and composition to be preserved (Figures S6–S8, Supporting Information). Figure 3 shows the high-resolution XPS spectra of the N 1s for six different samples synthesized in reaction mixtures containing progressively increasing concentrations of OAm and TOA. In all the spectra, two peaks, one centered near 396 eV and the other at 400 eV, were identified. According to numerous previous experimental and theoretical reports, the identity of the N environment associated with the N 1s peak around 396 eV is widely regarded as substitutional nitrogen located at an oxygen lattice site.<sup>21–31</sup> In TiN, the N 1s peak is positioned at 397.1 eV; slight variations in the Ti–N binding energy around this value are explained by the variation of the chemical environment and oxidation state as well as changes in the Fermi level of semiconducting  $N_{\text{sub}}\text{-TiO}_2$ .<sup>29,30</sup> Therefore, we positively assign the peak at 396 eV to  $N_{\text{sub}}$ . The N 1s peak located at 400 eV has been variously ascribed to different interstitial nitrogen species such as  $\text{NO}^{2-}$ ,  $\text{N}_2$ , and  $\text{NH}_x$ .<sup>21–31</sup> It is out of the scope of the present work to determine the exact chemical nature of the interstitial nitrogen species; however, consistent with

numerous previous reports, the N 1s peak at 400 eV can be positively attributed to interstitial nitrogen species  $N_{\text{int}}$ . In addition to nitrogen, signatures of charge compensating defects, namely, oxygen vacancies and  $\text{Ti}^{3+}$  centers, were observed by XPS and UV–vis absorption spectroscopy (Figures S4, S5, and S9, Supporting Information).<sup>21–31,47–49,51</sup>

As a general trend, higher  $N_{\text{tot}}$  and  $N_{\text{sub}}/N_{\text{tot}}$  ratio were measured in the presence of TOA. As the OAm concentration in the reaction mixture increased from 0.2 M in squalene to pure amine,  $N_{\text{tot}}$  raised from 2 to 6 at. % and the  $N_{\text{sub}}/N_{\text{tot}}$  ratio from 10 to 27% (Table S2, Supporting Information). When the primary OAm was substituted by the tertiary TOA, significantly higher  $N_{\text{tot}}$  and  $N_{\text{sub}}/N_{\text{tot}}$  ratio were measured, with  $N_{\text{tot}}$  and  $N_{\text{sub}}/N_{\text{tot}}$  reaching values as high as 17 at. % and 77% (Table S2, Supporting Information), respectively. In order to assess the role of the amine type on the nitrogen lattice site selectivity, we tested another primary and another tertiary amine, specifically DDA and THA. The choice of these two amines was mainly dictated by their boiling point, that had to be compatible with reaction temperatures close to 300 °C. Below this temperature, the nitrogen content measured in the presence of primary amines fell lower than 1 at. %. Because of the low signal-to-noise ratio in the XPS signal associated with such a low atomic concentration, any quantitative analysis of the  $N_{\text{sub}}/N_{\text{tot}}$  ratio in this case was prohibited, thus making higher reaction temperatures a requirement.  $N_{\text{sub}}/N_{\text{tot}}$  ratios of 10 and 64% were measured in the presence of DDA and THA, respectively, thus providing additional proof of tertiary amines leading to a higher  $N_{\text{sub}}/N_{\text{tot}}$  ratio (Figure S1, Supporting Information).

Surface segregation of the nitrogen species was excluded by performing angle-resolved XPS (ARXPS) measurements (Figure S10, Supporting Information). While rigorous quantification of ARXPS is complicated for nanoparticle systems and the dependence of photoemission spectra on takeoff angles may be reduced with increasing roughness,<sup>52,53</sup> qualitative assessment of the compositional uniformity within the nanoparticles can be positively assessed by this method. The angle-dependent concentration and ratio between substitutional and interstitial sites of N dopants observed by these

measurements were constant, thus providing supporting evidence for the presence of nitrogen throughout the volume of the nanocrystals.

XPS revealed our ability to control the nitrogen position at interstitial or substitutional sites of the  $\text{TiO}_2$  lattice by changing the amine type, as lower  $N_{\text{tot}}$  and  $N_{\text{sub}}/N_{\text{tot}}$  were measured with primary amines (i.e., OAm) versus tertiary amines (i.e., TOA). NMR and FTIR studies provided insights into the reaction mechanism by elucidating the key role played by the amines in this context.

Two different reaction pathways (A and B) were suggested by the NMR and FTIR data (Figures S11 and S12 and Scheme S1, Supporting Information). Mechanism A prevails in the presence of primary amines. Herein, the primary amines act as proton donors for  $\text{NaNH}_2$ , that is a strong base; thus, ammonia is generated in situ. The growth of the  $\text{TiO}_2$  lattice occurs by aminolysis of chlorotitanium carboxy complexes, in accordance with previous literature reports.<sup>54</sup> As mentioned in the Introduction, one of the most common routes to introduce nitrogen defects in oxides is by high temperature annealing of presynthesized metal oxides in ammonia flow. Also, oxynitride glass crystallization from metal-oxo gels by thermal annealing in ammonia has been reported.<sup>55</sup> If we assume a similar chemistry to proceed in our case, the  $\text{NH}_3$  generated in situ is then responsible for the introduction of nitrogen in the  $\text{TiO}_2$  nanostructures during their growth. Because oxygen replacement by nitrogen takes place at much higher temperatures (above 600 °C even in the nanosize regime)<sup>56,57</sup> than the growth temperature of the N- $\text{TiO}_2$  NUs, mainly interstitial nitrogen species are expected as a result of  $\text{TiO}_2$  nanostructures growing in the presence of  $\text{NH}_3$ . This is consistent with what is shown by the XPS results in the presence of primary amines.

Tertiary amines do not act as proton donors. While some ammonia is still being generated in situ by the reaction of  $\text{NaNH}_2$  with oleic acid (in trace amount), mechanism B relies mainly on the formation of  $\text{TiCl}_{4-x}(\text{NH}_2)_x$  complexes from the reaction between  $\text{TiCl}_4$  and  $\text{NaNH}_2$ , the latter being an excellent nucleophile in addition to a strong base.<sup>58</sup> These  $\text{TiCl}_{4-x}(\text{NH}_2)_x$  complexes can undergo a self-condensation reaction or condense with the chlorotitanium carboxylate derivatives to form an extended O–Ti–N network. The latter then crystallizes in the N- $\text{TiO}_2$  NUs with the nitrogen impurities occupying mainly substitutional sites.<sup>59–62</sup> This sol–gel polycondensation chemistry has been largely demonstrated in the case of metal oxide nanocrystals; more recently, an analogous nonoxide sol–gel chemistry has been tested for the synthesis of  $\text{TiN}$  and  $\text{Ta}_3\text{N}_5$ .<sup>59–62</sup> The size dependence of the crystallization temperature can explain the lower crystallization temperature of our work compared with the bulk counterparts, similarly to what has been postulated for metal oxide and other classes of nanocrystals.<sup>54,63</sup>

Consistent with many reports about nanocrystal doping, we refer to mechanism A as “growth-doping”, because N atoms are introduced during the growth of the  $\text{TiO}_2$  nanostructures by the ammonia generated in situ, and to mechanism B as “nucleation-doping”, because of the formation of Ti–N bonds during earlier stages of the synthesis.<sup>6,64–68</sup> To summarize, we suggest the “nucleation-doping” and the “growth-doping” to prevail in the presence of tertiary and primary amines, respectively.

The validity of our mechanistic understanding was further confirmed by the kinetic evolution of the nitrogen content that was monitored by XPS. Figure 4 shows  $N_{\text{tot}}$  in aliquots

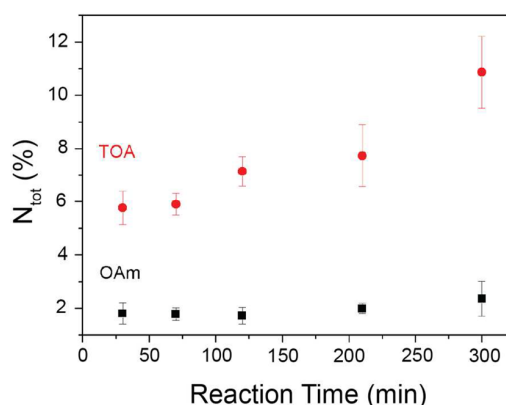


**Figure 4.**  $N_{\text{tot}}$  versus reaction time from XPS measurements carried out on aliquots collected during N- $\text{TiO}_2$  NU synthesis in pure TOA (red) and OAm (black).

collected at different times from samples synthesized using OAm and TOA as the solvent. First, it should be noticed that in TOA  $N_{\text{tot}}$  is much higher at the earliest evolution stages compared to OAm ( $\approx 6$  at. % versus 2 at. % after 30 min). Second, the nitrogen incorporation rate is time-dependent in TOA, while it appears to be constant over time in the presence of OAm. The steeper increase of  $N_{\text{tot}}$  with TOA indicates that more nitrogen is introduced in the lattice during the nucleation stage, consistently with the proposed nucleation doping mechanism. As for the time dependence of the N incorporation rate, we hypothesize the following. In the case of OAm, the ammonia generated in situ is expected to evolve quickly from the system. Therefore, the steady state for the doping incorporation reaction is reached during the early stages of the growth. Specifically, we found the nitrogen concentration to plateau after the first 30 min. In the case of TOA, the  $\text{TiCl}_{4-x}(\text{NH}_2)_x$  monomers form in the reaction mixture. As the solution starts to be depleted of the titanium–carboxylate complexes, that are the  $\text{TiO}_2$  lattice nutrients, the condensation of the  $\text{TiCl}_{4-x}(\text{NH}_2)_x$  (see Scheme S1, Supporting Information) becomes kinetically more competitive, thus resulting in more N dopants being incorporated as the reaction progresses. A similar kinetic evolution has been observed for other doped nanocrystal systems as well.<sup>1</sup>

To investigate the effect of nitrogen doping concentration and lattice occupational site on the optoelectronic properties of the N- $\text{TiO}_2$  NUs, the optical band gap was estimated by UV–vis diffuse reflectance spectroscopy and the presence of additional electronic states above the valence band was investigated by XPS (Figure 5 and Figures S13–S16, Supporting Information). With the purpose to highlight the main differences between substitutionally and interstitially doped samples, Figure 5a shows the UV–vis absorption spectra corresponding to two of the N- $\text{TiO}_2$  samples with the lowest ( $N_{\text{int}}$ -rich) and highest ( $N_{\text{sub}}$ -rich) substitutional nitrogen concentration. Specifically, the  $N_{\text{int}}$ -rich sample corresponds to a NU sample synthesized in 0.2 M OAm and possesses a  $N_{\text{sub}}/N_{\text{tot}}$  ratio equals to 10%; the  $N_{\text{sub}}$ -rich sample was synthesized in TOA and contains a  $N_{\text{sub}}/N_{\text{tot}}$  ratio equal to 74%. While for both samples a shoulder in the visible region between 400 and 500 nm was observed, the  $N_{\text{sub}}$ -rich sample differed from the  $N_{\text{int}}$ -rich sample by exhibiting an absorption tail extended to longer wavelengths in the visible range and a red-shifted absorption edge. The Tauc plot analysis (Figure

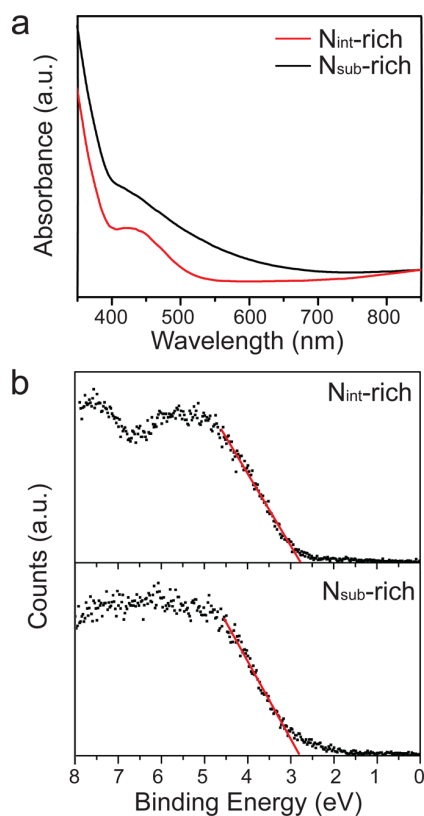


**Figure 5.** Optoelectronic properties of N-TiO<sub>2</sub> NUs. UV-vis absorption spectra (a) and VB XPS spectra (b) of N-TiO<sub>2</sub> NUs containing  $N_{\text{tot}} = 5$  at. % and  $N_{\text{sub}}/N_{\text{int}} = 10\%$  ( $N_{\text{int}}\text{-rich}$ ) and  $N_{\text{tot}} = 17$  at. % and  $N_{\text{sub}}/N_{\text{int}} = 74\%$  ( $N_{\text{sub}}\text{-rich}$ ). Red lines in panel b are linear regressions used to indicate the valence band edge position at 2.9 eV for  $N_{\text{int}}\text{-rich}$  and 2.85 eV for  $N_{\text{sub}}\text{-rich}$ .

S13, Supporting Information) yielded to band gaps of 2.7 and 2.5 eV for the  $N_{\text{int}}\text{-rich}$  and  $N_{\text{sub}}\text{-rich}$  samples, respectively, both reduced when compared to the 2.9 eV indirect band gap measured for pure rutile TiO<sub>2</sub> (Figure S14, Supporting Information). These optical features were in accordance with the yellow color of the N-TiO<sub>2</sub> NU dispersions (Figure S15, Supporting Information) and were similar to those reported in previous work on rutile N-TiO<sub>2</sub> synthesized by sputtering or annealing in ammonia flow.<sup>17,23,69,70</sup>

As for the nature of the TiO<sub>2</sub> rutile band gap, some ambiguity can be found in the literature, probably due to the fact that it has energetically close lying indirect and direct transitions.<sup>71</sup> In this work, the quadratic dependence of the absorption coefficient on the excitation energy is consistent with an indirect band gap, in agreement with the data reported by others for N-doped rutile TiO<sub>2</sub>.<sup>69</sup>

The XPS VB spectra of all samples (Figure 5b and Figure S16, Supporting Information) showed a tail in the range 0–1 eV above the VB edge with increasing spectral contribution as  $N_{\text{tot}}$  and  $N_{\text{sub}}/N_{\text{tot}}$  increase. Additionally, the characteristic two peaks in the VB structure of rutile TiO<sub>2</sub> (at 5 and 7.5 eV),<sup>47,48</sup> still present in the  $N_{\text{int}}\text{-rich}$  samples, became less pronounced in the  $N_{\text{sub}}\text{-rich}$  samples. Many studies have addressed the question of the character, localized or delocalized, of the electronic states associated with the N impurities, but no general consensus has been reached yet.<sup>17,18,28,69</sup> While some authors claim that the band gap of the solid is reduced due to a

rigid valence band shift upon doping, others attribute the observed absorption of visible light by N-TiO<sub>2</sub> to the excitation of electrons from shallow electronic states just above the TiO<sub>2</sub> VB.<sup>17,18,28,69</sup> In some cases, a slight increase of the optical gap has even been observed for the rutile polymorphs.<sup>72</sup> In our work, the tailing of the VB structure at lower binding energies observed by the VB XPS measurements indicates that additional electronic states above the VB edge accompany the incorporation of the nitrogen dopants in the N-TiO<sub>2</sub> NUs, consistent with the hybridization of less tightly bound N 2p levels with O 2p levels causing a reduction in bandgap.<sup>49</sup> We do not comment about the absolute positions of the VB edge in Figure 5b and Figure S16 (Supporting Information), as they are referenced to the Fermi level, set at binding energy equal to zero, which shifts with doping as well. The complex dependence of the Fermi energy with the defect type and charge state (N<sup>3-</sup>, Ti<sup>3+</sup>, oxygen vacancies) requires further studies to establish a precise correlation between the VB edge absolute position and the nitrogen content. As for the loss of the extended structure within the VB with the  $N_{\text{sub}}/N_{\text{tot}}$  increase, it is in agreement with the progressive increase of the local lattice disorder associated with high defect densities, as reported in previous work.<sup>47,49</sup>

Despite the ongoing debate regarding the exact nature of the absorption edge red shift in N-modified TiO<sub>2</sub>, it is of general agreement that extending light absorption to the visible range by doping has limited benefit for the photocatalytic activity if only highly localized states are generated. To demonstrate the feasibility of integrating the N-TiO<sub>2</sub> NUs in a photoelectrochemical device so as to correlate the change of the electronic band structure associated with the introduction of N dopants to the photocatalytic activity, we assembled photoelectrodes from our N-TiO<sub>2</sub> NU dispersions. We then tested the N-TiO<sub>2</sub> NU films as photoanodes for water oxidation in technologically relevant conditions and in the absence of sacrificial agents.

The current density–voltage ( $J$ – $V$ ) characteristics measured for typical  $N_{\text{int}}\text{-rich}$  and  $N_{\text{sub}}\text{-rich}$  samples are reported in Figure S17 (Supporting Information). While the total photocurrent densities under simulated solar illumination and under UV-only irradiation (Table S3, Supporting Information) were similar for both samples, the photocurrent drop with a 400 nm cutoff filter inserted was much lower for the  $N_{\text{sub}}\text{-rich}$  TiO<sub>2</sub> photoelectrode compared to  $N_{\text{int}}\text{-rich}$  TiO<sub>2</sub> (50 and 88%, respectively). Further investigations are needed and will be pursued in future work to truly unravel the underlying electronic structure modifications and the associated mechanism responsible for the different photocatalytic behavior of the  $N_{\text{sub}}\text{-rich}$  N-TiO<sub>2</sub> and the  $N_{\text{int}}\text{-rich}$  N-TiO<sub>2</sub> NUs. However, the results obtained so far suggest that the band gap reduction observed in the case of the  $N_{\text{sub}}\text{-rich}$  TiO<sub>2</sub> NUs is accompanied by delocalized valence band states that enabled generation and transport of active charge carriers to the surface under the visible light illumination.

## CONCLUSIONS

In summary, we have developed a wet-chemistry synthetic approach to manipulate the occupational lattice sites of nitrogen dopants and their content in highly branched rutile TiO<sub>2</sub> nanostructures. The  $N_{\text{sub}}/N_{\text{tot}}$  ratio was varied from 10 to 77% while the total nitrogen atomic content  $N_{\text{tot}}$  spanned from 2 to 17 at. %, with higher concentration accompanying higher  $N_{\text{sub}}/N_{\text{tot}}$  ratios. Even for such a high nitrogen content, the TiO<sub>2</sub> NUs persisted in a heavily doping regime, as no titanium

oxynitride phase was observed. The unprecedented structural and compositional tunability shown in this work was enabled by a fundamental understanding of the chemistry behind doping. We showed that a nucleation-doping mechanism, triggered by tertiary amines, and a growth-doping mechanism, which dominates when primary amines are used instead, drive the introduction of nitrogen impurities in substitutional or interstitial sites, respectively. By briefly discussing our results when testing the N-TiO<sub>2</sub> NUs as photoanodes for water oxidation, we demonstrate the potential of the N-TiO<sub>2</sub> NUs to build a meaningful correlation between the dopant concentration and occupational lattice sites and practical solar water oxidation function. Although there have been numerous attempts in the literature to compare interstitial and substitutional nitrogen-doped TiO<sub>2</sub>, we believe the discrepancy among the reported results to be due to the necessity of resorting to different preparation methods to cover a wide compositional range. Despite our initial focus on N-doped TiO<sub>2</sub>, our chemistry-driven doping approach is potentially applicable across a wider range of doped systems and is expected to provide a route to understanding and controlling structure/function relationships, which are often prevented by a generally poor angstrom-scale material control.

## ■ ASSOCIATED CONTENT

### ■ Supporting Information

Morphological and compositional analysis of N-TiO<sub>2</sub> samples during film processing for XPS analysis and photoelectrode preparation, TEM of time aliquots, characterization of N-TiO<sub>2</sub> samples with different primary and tertiary amines, NMR analysis of gas evolving from synthesis, FTIR analysis, ARXPS, VB XPS of all samples, and reaction schemes. This material is available free of charge via the Internet at <http://pubs.acs.org>.

## ■ AUTHOR INFORMATION

### ■ Corresponding Author

\*E-mail: [rbuonsanti@lbl.gov](mailto:rbuonsanti@lbl.gov). Phone: +1 510-495-8711.

### ■ Notes

The authors declare no competing financial interest.

## ■ ACKNOWLEDGMENTS

This material is based upon work performed by the Joint Center for Artificial Photosynthesis, a DOE Energy Innovation Hub, supported through the Office of Science of the U.S. Department of Energy under Award Number DE-SC0004993. We thank Dr. S. Aloni for his assistance in the high resolution TEM measurements performed under the Molecular Foundry user program and Dr. L. Trotochaud and Dr. F. Toma for useful discussions. Work at the Molecular Foundry was supported by the Office of Science, Office of Basic Energy Sciences, of the U.S. Department of Energy under Contract No. DE-AC02-05CH1123.

## ■ REFERENCES

- (1) Bryan, J. D.; Gamelin, D. R. Doped Semiconductor Nanocrystals: Synthesis, Characterization, Physical Properties, and Applications. *Prog. Inorg. Chem.* **2005**, *54*, 47–126.
- (2) Norris, D. J.; Efros, A. L.; Erwin, S. C. Doped Nanocrystals. *Science* **2008**, *319*, 1776–1779.
- (3) Sahu, A.; Kang, M. S.; Kompch, A.; Notthoff, C.; Wills, A. W.; Deng, D.; Winterer, M.; Frisbie, C. D.; Norris, D. J. Electronic Impurity Doping in CdSe Nanocrystals. *Nano Lett.* **2012**, *12*, 2587–2594.
- (4) Luther, J. M.; Jain, P. K.; Ewers, T.; Alivisatos, A. P. Localized Surface Plasmon Resonances Arising from Free Carriers in Doped Quantum Dots. *Nat. Mater.* **2011**, *10*, 361–366.
- (5) Beaulac, R.; Ochsenbein, S. T.; Gamelin, D. R. In *Nanocrystal Quantum Dots*; Klimov, I. V., Ed.; Taylor & Francis: New York, 2010; pp 397–453.
- (6) Buonsanti, R.; Milliron, D. J. Chemistry of Doped Nanocrystals. *Chem. Mater.* **2013**, *25*, 1305–1317.
- (7) Buonsanti, R.; Llordes, A.; Aloni, S.; Helms, B. A.; Milliron, D. J. Tunable Infrared Absorption and Visible Transparency of Colloidal Aluminum-Doped Zinc Oxide Nanocrystals. *Nano Lett.* **2011**, *11*, 4706–4710.
- (8) Lounis, S. D.; Runnerstrom, E. L.; Bergerud, A.; Nordlund, D.; Milliron, D. J. Influence of Dopant Distribution on the Plasmonic Properties of Indium Tin Oxide Nanocrystals. *J. Am. Chem. Soc.* **2014**, *136*, 7110–7116.
- (9) Garcia, G.; Buonsanti, R.; Runnerstrom, E. L.; Mendelsberg, R. J.; Llordes, A.; Anders, A.; Richardson, T. J.; Milliron, D. J. Dynamically Modulating the Surface Plasmon Resonance of Doped Semiconductor Nanocrystals. *Nano Lett.* **2011**, *11*, 4415–4420.
- (10) De Trizio, L.; Buonsanti, R.; Schimpf, A. M.; Llordes, A.; Gamelin, D. R.; Simonutti, R.; Milliron, D. J. Nb-Doped Colloidal TiO<sub>2</sub> Nanocrystals with Tunable Infrared Absorption. *Chem. Mater.* **2013**, *25*, 3383–3390.
- (11) Li, X.; Wang, R.; Zhang, F.; Zhao, D. Engineering Homogeneous Doping in Single Nanoparticle To Enhance Upconversion Efficiency. *Nano Lett.* **2014**, *14*, 3634–3639.
- (12) Chan, E. M.; Han, G.; Goldberg, J. D.; Gargas, D. J.; Ostrowski, A. D.; Schuck, P. J.; Cohen, B. E.; Milliron, D. J. Combinatorial Discovery of Lanthanide-Doped Nanocrystals with Spectrally Pure Upconverted Emission. *Nano Lett.* **2012**, *12*, 3839–3845.
- (13) Asahi, R.; Morikawa, T.; Ohwaki, T.; Aoki, K.; Taga, Y. Visible-Light Photocatalysis in Nitrogen-Doped Titanium Oxides. *Science* **2001**, *293*, 269–271.
- (14) Cole, B.; Marsen, B.; Miller, E.; Yan, Y.; To, B.; Jones, K.; Al-Jassim, M. Evaluation of Nitrogen Doping of Tungsten Oxide for Photoelectrochemical Water Splitting. *J. Phys. Chem. C* **2008**, *112*, 5213–5220.
- (15) Liu, G.; Wang, L.; Sun, C.; Yan, X.; Wang, X.; Chen, Z.; Smith, S. C.; Cheng, H.-m.; Lu, G. Q. Band-to-Band Visible-Light Photon Excitation and Photoactivity Induced by Homogeneous Nitrogen Doping in Layered Titanates. *Chem. Mater.* **2009**, *21*, 1266–1274.
- (16) Wu, Y.; Lazic, P.; Hautier, G.; Persson, K.; Ceder, G. First Principles High Throughput Screening of Oxynitrides for Water-Splitting Photocatalysts. *Energy Environ. Sci.* **2013**, *6*, 157–168.
- (17) Asahi, R.; Morikawa, T.; Irie, H.; Ohwaki, T. Nitrogen-Doped Titanium Dioxide as Visible-Light-Sensitive Photocatalyst: Designs, Developments, and Prospects. *Chem. Rev.* **2014**, *114*, 9824–9852.
- (18) Di Valentin, C.; Finazzi, E.; Pacchioni, G.; Selloni, A.; Livraghi, S.; Paganini, M. C.; Giamello, E. N-Doped TiO<sub>2</sub>: Theory and Experiment. *Chem. Phys.* **2007**, *339*, 44–56.
- (19) Cao, J.; Zhang, Y.; Tong, H.; Li, P.; Kako, T.; Ye, J. Selective Local Nitrogen Doping in a TiO<sub>2</sub> Electrode for Enhancing Photoelectrochemical Water Splitting. *Chem. Commun.* **2012**, *48*, 8649–8651.
- (20) Zhao, Z.; Li, Z.; Zou, Z. Water Adsorption and Decomposition on N/V-Doped Anatase TiO<sub>2</sub> (101) Surfaces. *J. Phys. Chem. C* **2013**, *117*, 6172–6184.
- (21) Livraghi, S.; Chierotti, M. R.; Giamello, E.; Magnacca, G.; Paganini, M. C.; Cappelletti, G.; Bianchi, C. L. Nitrogen-Doped Titanium Dioxide Active in Photocatalytic Reactions with Visible Light: A Multi-Technique Characterization of Differently Prepared Materials. *J. Phys. Chem. C* **2008**, *112*, 17244–17252.
- (22) Zhang, Z.; Wang, X.; Long, J.; Gu, Q.; Ding, Z.; Fu, X. Nitrogen-doped Titanium Dioxide Visible Light Photocatalyst: Spectroscopic Identification of Photoactive Centers. *J. Catal.* **2010**, *276*, 201–214.

- (23) Torres, G. R.; Lindgren, T.; Lu, J.; Granqvist, C. G.; Lindquist, S. E. Photoelectrochemical Study of Nitrogen-Doped Titanium Dioxide for Water Oxidation. *J. Phys. Chem. B* **2004**, *108*, 5995–6003.
- (24) Chen, C.; Bai, H.; Chang, C. Effect of Plasma Processing Gas Composition on the Nitrogen Doping Status and Visible Light Photocatalysis of TiO<sub>2</sub>. *J. Phys. Chem. C* **2007**, *111*, 15228–15235.
- (25) Livraghi, S.; Paganini, M. C.; Giamello, E.; Selloni, A.; Di Valentin, C.; Pacchioni, G. Origin of Photoactivity of Nitrogen-Doped Titanium Dioxide under Visible Light. *J. Am. Chem. Soc.* **2006**, *128*, 15666–15671.
- (26) Irie, H.; Watanabe, Y.; Hashimoto, K.; Hashimoto, K. Nitrogen-Concentration Dependence on Photocatalytic Activity of TiO<sub>2-x</sub>N<sub>x</sub> Powders. *J. Phys. Chem. B* **2003**, *107*, 5483–5486.
- (27) Cheung, S. H.; Nachimuthu, P.; Joly, A. G.; Engelhard, M. H.; Bowman, M. K.; Chambers, S. A. N Incorporation and Electronic Structure in N-doped TiO<sub>2</sub> (110) Rutile. *Surf. Sci.* **2007**, *601*, 1754–1762.
- (28) Di Valentin, C.; Pacchioni, G.; Selloni, A.; Livraghi, S.; Giamello, E. Characterization of Paramagnetic Species in N-doped TiO<sub>2</sub> Powders by EPR Spectroscopy and DFT. *J. Phys. Chem. B* **2005**, *109*, 11414–11419.
- (29) Delfino, M.; Fair, J. A.; Hodul, D. J. X-Ray Photoemission Spectra of Reactively Sputtered TiN. *Appl. Phys.* **1992**, *71*, 6079–6085.
- (30) Saha, N. C.; Tompkins, H. G. Titanium Nitride Oxidation Chemistry: An X-ray Photoelectron Spectroscopy Study. *J. Appl. Phys.* **1992**, *72*, 3072–3079.
- (31) Diwald, O.; Thompson, T. L.; Zubkov, T.; Goralski, E. G.; Walck, S. D.; Yates, J. T. Photochemical Activity of Nitrogen Doped Rutile TiO<sub>2</sub> in Visible Light. *J. Phys. Chem. B* **2004**, *108*, 6004–6008.
- (32) M. Cargnello, M.; Gordon, T. R.; Murray, C. B. Solution-Phase Synthesis of Titanium Dioxide Nanoparticles and Nanocrystals. *Chem. Rev.* **2014**, *114*, 9319–9345.
- (33) Liu, L.; Chen, X. Titanium Dioxide Nanomaterials: Self-Structural Modifications. *Chem. Rev.* **2014**, *114*, 9890–9918.
- (34) De Angelis, F.; Di Valentin, C.; Fantacci, S.; Vittadini, A.; Selloni, A. Theoretical Studies on Anatase and Less Common TiO<sub>2</sub> Phases: Bulk, Surfaces, and Nanomaterials. *Chem. Rev.* **2014**, *114*, 9708–9753.
- (35) Hu, S.; Shaner, M. R.; Beardslee, J. A.; Lichterman, M.; Brunschwig, B. S.; Lewis, N. S. Amorphous TiO<sub>2</sub> Coatings Stabilize Si, GaAs, and GaP Photoanodes for Efficient Water Oxidation. *Science* **2014**, *344*, 1005–1009.
- (36) Cong, Y.; Zhang, J.; Chen, F.; Anpo, M. Synthesis and Characterization of Nitrogen Doped Nanophotocatalyst with High Visible Light Activity. *J. Phys. Chem. C* **2007**, *111*, 6976–6982.
- (37) Lopez-Luke, T.; Wolcott, A.; Xu, L.-p.; Chen, S.; Wen, Z.; Li, J.; Rosa, E. R.; Zhang, J. Z. Nitrogen Doped and CdSe Sensitized Nanocrystalline TiO<sub>2</sub>. *J. Phys. Chem. C* **2008**, *112*, 1282–1292.
- (38) Burda, C.; Lou, Y. B.; Chen, X. B.; Samia, A. C. S.; Stout, J.; Gole, J. L. Enhanced Nitrogen Doping in TiO<sub>2</sub> Nanoparticles. *Nano Lett.* **2003**, *3*, 1049–1051.
- (39) Qiu, X.; Burda, C. Chemically Synthesized Nitrogen-Doped Metal Oxide Nanoparticles. *Chem. Phys.* **2007**, *339*, 1–10.
- (40) Rosen, E. L.; Buonsanti, R.; Llordes, A.; Sawvel, A. M.; Milliron, D. J.; Helms, B. A. Exceptionally Mild Reactive Stripping of Native Ligands from Nanocrystal Surfaces by Using Meerwein's Salt. *Angew. Chem., Int. Ed.* **2012**, *51*, 684–689.
- (41) Jun, Y.-w.; Chung, H.-W.; Jang, J.-t.; Cheon, J. Multiple Twinning Drives Nanoscale Hyper-branching of Titanium Dioxide Nanocrystals. *J. Mater. Chem.* **2011**, *21*, 10283–10286.
- (42) Buonsanti, R.; Carlino, E.; Giannini, C.; Altamura, D.; Marco, L.; Giannuzzi, R.; Manca, M.; Gigli, G.; Cozzoli, P. D. Hyperbranched Anatase TiO<sub>2</sub> Nanocrystals: Nonaqueous Synthesis, Growth Mechanism, and Exploitation in Dye-Sensitized Solar Cells. *J. Am. Chem. Soc.* **2011**, *133*, 19216–19239.
- (43) Kanaras, A. G.; Sonnichsen, C.; Liu, H. T.; Alivisatos, A. P. Controlled Synthesis of Hyperbranched Inorganic Nanocrystals with Rich Three-Dimensional Structures. *Nano Lett.* **2005**, *5*, 2164–2167.
- (44) Zhang, H.; Ha, D.-H.; Hovden, R.; Kourkoutis, L. F.; Robinson, R. D. Controlled Synthesis of Uniform Cobalt Phosphide Hyperbranched Nanocrystals Using Tri-n-octylphosphine Oxide as a Phosphorus Source. *Nano Lett.* **2011**, *11*, 188–197.
- (45) Tang, J.; Alivisatos, A. P. Crystal Splitting in the Growth of Bi<sub>2</sub>S<sub>3</sub>. *Nano Lett.* **2006**, *6*, 2701–2706.
- (46) Lo Presti, L.; Ceotto, M.; Spadavecchia, F.; Cappelletti, G.; Meroni, D.; Acres, R. G.; Ardzzone, S. Role of the Nitrogen Source in Determining Structure and Morphology of N-Doped Nanocrystalline TiO<sub>2</sub>. *J. Phys. Chem. C* **2014**, *118*, 4797–4807.
- (47) Batzill, M.; Morales, E. H.; Diebold, U. Influence of Nitrogen Doping on Defect Formation in Anatase and Rutile. *Phys. Rev. Lett.* **2006**, *96*, 026103.
- (48) Graciani, J.; Alvarez, L. J.; Rodriguez, J. A.; Sanz, J. F. N Doping of Rutile TiO<sub>2</sub> (110) Surface. A Theoretical DFT Study. *J. Phys. Chem. C* **2008**, *112*, 2624–2631.
- (49) Rumaiz, A. K.; Woicik, J. C.; Cockayne, E.; Lin, H. Y.; Jaffari, G. H.; Shah, S. I. Oxygen Vacancies in N doped Anatase TiO<sub>2</sub>: Experiment and First-Principles Calculations. *Appl. Phys. Lett.* **2009**, *95*, 262111–262113.
- (50) Varghese, S.; David, M.; Barry, C. M.; Alexei, K.; Leonid, S. D.; Qing, D.; Vladimir, D. Nonlinear Size Dependence of Anatase TiO<sub>2</sub> Lattice Parameters. *Appl. Phys. Lett.* **2006**, *88*, 243103.
- (51) Prokes, S. M.; Gole, J. L.; Chen, X. B.; Burda, C.; Carlos, W. E. Defect-Related Optical Behavior in Surface Modified TiO<sub>2</sub> Nanostructures. *Adv. Funct. Mater.* **2005**, *15*, 161–167.
- (52) Oswald, S.; Oswald, F. Modeling of Complex Surface Structures for ARXPS. *Surf. Interface Anal.* **2008**, *40*, 700–705.
- (53) Kappen, P.; Reihls, K.; Seidel, C.; Voetz, M.; Fuchs, H. Overlayer Thickness Determination by Angular Dependent X-ray Photoelectron Spectroscopy (ADXPS) of Rough Surfaces with a Spherical Topography. *Surf. Sci.* **2000**, *465*, 40–50.
- (54) Buonsanti, R.; Grillo, V.; Carlino, E.; Giannini, C.; Kipp, T.; Cingolani, R.; Cozzoli, P. D. Nonhydrolytic Synthesis of High-Quality Anisotropically Shaped Brookite TiO<sub>2</sub> Nanocrystals. *J. Am. Chem. Soc.* **2008**, *130*, 11223–11233.
- (55) Brinker, C. J.; Haaland, D. M. Oxynitride Glass-Formation from Gels. *J. Am. Ceram. Soc.* **1983**, *66*, 758–765.
- (56) Martinez-Ferrero, E.; Sakatani, Y.; Boissiere, C.; Grosso, D.; Fuertes, A.; Fraxedas, J.; Sanchez, C. Nanostructured Titanium Oxynitride Porous Thin Films as Efficient Visible-Active Photocatalysts. *Adv. Funct. Mater.* **2007**, *17*, 3348–3354.
- (57) Grasset, F.; Starukh, G.; Spanhel, L.; Ababou-Girand, S.; Su, D.-S.; Klein, A. From ZnO Colloids to Nanocrystalline Colored Zn<sub>x</sub>Ti<sub>1-x</sub>O<sub>w-z</sub>N<sub>z</sub> Spinel Films. *Adv. Mater.* **2005**, *17*, 294–297.
- (58) Fowles, G. W. A.; Nicholis, Q. D. Inorganic Reactions in Liquid Ammonia. *Rev. Chem. Soc.* **1962**, *16*, 19–43.
- (59) Cozzoli, P. D.; Kornowski, A.; Weller, H. Low-Temperature Synthesis of Soluble and Processable Organic-Capped Anatase TiO<sub>2</sub> Nanorods. *J. Am. Chem. Soc.* **2003**, *125*, 14539–14548.
- (60) Mallinson, C. F.; Gray, B. M.; Hector, A. L.; McLachlan, M. A.; Owen, J. R. Chemical Vapor Deposition of Vanadium, Niobium, and Tantalum Nitride Thin Films. *Inorg. Chem.* **2013**, *52*, 9994–9999.
- (61) Gray, B. M.; Hassan, S.; Hector, A. L.; Kalaji, A.; Mazumder, B. Template Infiltration Routes to Ordered Macroporous TiN and SiN<sub>x</sub> Films. *Chem. Mater.* **2009**, *21*, 4210–4215.
- (62) Jackson, A. W.; Hector, A. L. A Nonoxidic Sol-gel Route to Titanium Nitride and Carbonitride films by Primary Amine Condensation. *J. Mater. Chem.* **2007**, *17*, 1016–1022.
- (63) Hirasawa, M.; Orii, T.; Seto, T. Size-dependent Crystallization of Si Nanoparticles. *Appl. Phys. Lett.* **2006**, *88*, 093119.
- (64) Chen, D.; Viswanatha, R.; Ong, G. L.; Xie, R.; Balasubramanian, M.; Peng, X. Temperature Dependence of “Elementary Processes” in Doping Semiconductor Nanocrystals. *J. Am. Chem. Soc.* **2009**, *131*, 9333–9339.
- (65) Pradhan, N.; Peng, X. Efficient and Color-Tunable Mn-Doped ZnSe Nanocrystal Emitters: Control of Optical Performance via Greener Synthetic Chemistry. *J. Am. Chem. Soc.* **2007**, *129*, 3339–3347.

- (66) Pradhan, N.; Goorskey, D.; Thessing, J.; Peng, X. G. An Alternative of CdSe Nanocrystal Emitters: Pure and Tunable Impurity Emissions in ZnSe Nanocrystals. *J. Am. Chem. Soc.* **2005**, *127*, 17586–17587.
- (67) Yang, Y. A.; Chen, O.; Angerhofer, A.; Cao, Y. C. On Doping CdS/ZnS Core/Shell Nanocrystals with Mn. *J. Am. Chem. Soc.* **2008**, *130*, 15649–15661.
- (68) Yang, Y. A.; Chen, O.; Angerhofer, A.; Cao, Y. C. Radial-position-controlled Doping in CdS/ZnS core/shell Nanocrystals. *J. Am. Chem. Soc.* **2006**, *128*, 12428–12429.
- (69) Hoang, S.; Guo, S.; Hahn, N. T.; Bard, A. J.; Mullins, C. B. Visible Light Driven Photoelectrochemical Water Oxidation on Nitrogen-Modified TiO<sub>2</sub> Nanowires. *Nano Lett.* **2012**, *12*, 26–32.
- (70) Hoang, S.; Berglund, S. P.; Hahn, N. T.; Bard, A. J.; Mullins, C. B. Enhancing Visible Light Photo-oxidation of Water with TiO<sub>2</sub> Nanowire Arrays via Cotreatment with H<sub>2</sub> and NH<sub>3</sub>: Synergistic Effects between Ti<sup>3+</sup> and N. *J. Am. Chem. Soc.* **2012**, *134*, 3659–3662.
- (71) Luttrell, T.; Halpegamage, S.; Tao, J.; Kramer, A.; Sutter, E.; Batzill, M. Why is Anatase a Better Photocatalyst than Rutile? - Model Studies on Epitaxial TiO<sub>2</sub> Films. *Sci. Rep.* **2014**, *4*, 4043.
- (72) Diwald, O.; Thompson, T. L.; Zubkov, T.; Goralski, E. G.; Walck, S. D.; Yates, J. T. The Effect of Nitrogen Ion Implantation on the Photoactivity of TiO<sub>2</sub> Rutile Single Crystals. *J. Phys. Chem. B* **2004**, *108*, 52–57.